Int. J. Heat Mass Transfer. Vol. 35, No. 2, pp. 307–317, 1992
Printed in Great Britain

0017–9310/92 $5.00 + 0.00

Research on hydrodynamics and heat transfer for fluid flow around heating spheres in tandem

BU-XUAN WANG and TAO LIU
Thermal Engineering Department, Tsinghua University, Beijing 100084, China

(*Received* 10 *January* 1991 *and in final form* 3 *April* 1991)

Abstract—The temperature field and heat transfer for fluid flow around the heating solid spheres in tandem have been measured by laser holographic interferometry together with an infrared scanning technique. The heat transfer characteristics for heating solid spheres with equal or unequal diameters as affected by various parameters such as Re, ΔT, x and d_2/d_1 are obtained experimentally in detail. The numerical simulation has been made to predict conditions of constant and variable physical properties. The numerical results are quite close to the experimental ones, and show that more systematic and audio–visual results can be obtained.

1. INTRODUCTION

THE INVESTIGATION of two phase flow, heat transfer and combustion of particulate systems is technically important to many engineering problems such as in developing new coal combustion circulating fluidized beds, fluidized- and fixed-bed chemical reactors, as well as the pneumatic transportation of solids, etc. To study progressively such complicated systems, single or several particles have to be extracted from the system to be an object of study. Many results have been reported in the literature on the analytical solution for the steady creeping flow around a solid sphere [1] since Stokes, and very recently, multi-particle systems with mutual interaction have also been studied [2]. In general, however, such analytical solutions in the literature are available for the situation where $Re < 1$, i.e. for creeping flow only. It is difficult to obtain useful analytical results in engineering practice where the range of Re is much wider, particularly for heat and mass transfer.

There have been many experimental results about the drag factor, heat transfer and mass transfer characteristics for the flow around a single sphere, which are helpful in the study of multi-particle systems, and are summarized in ref. [1], where different empirical correlations were recommended for corresponding parameter ranges to obtain results as satisfactory as possible. However, experimental study of multi-particle systems, especially related to mutual interaction, are scarcely reported, and restrained in flow pattern and drag factor [3–5] without heat and mass transfer. Sparrow and Prieto [6] measured the Sherwood number, Sh, for two contacted unheating spheres and obtained the corresponding empirical correlation of the Nusselt number, Nu, by means of heat and mass transfer analogy. Such a situation is unfavorable for verifying analytical and numerical results, and, therefore, limits the possible progress of theoretical investigation.

We have carried out experiments on fluid flow and heat transfer around heating spheres with mutual interaction to provide a sound basis for numerical simulation. The fluid temperature fields around spheres were measured with a laser holographic technique while the temperature distribution on the sphere surface was measured with an infrared scanning technique. Different affecting parameters were taken into consideration to simulate the combustion of suspended particles more closely. However, it is not realistic to obtain more systematic results through experiments due to the limit on the number of experimental conditions and the amount of work. Hence, numerical simulation verified by necessary experiments acts as an effective means to get much more extended results.

Many numerical results have been reported for fluid flow around spheres in the literature because of the rapid progress of computer science and advances in numerical methods. The state-of-the-art has been reviewed in ref. [7]. In general, the previous numerical simulations are mostly restrained to the cases of $Re < 200$ and the temperature range is quite narrow, so that the stream function–vorticity method is mostly used, with fluid thermophysical properties such as density, ρ, specific heat, c_p, and viscosity, μ, being assumed constant. During the real combustion process, temperature effects and hence variations in thermophysical properties should not be neglected. In the present work, the cylindrical cell model [8] is chosen to solve the problem numerically, which is physically reasonable and can be used over quite a wide range with less computation than in the three-dimensional method. By comparing the calculated results with experimental ones, the reliability of the physico-mathematical model adopted for numerical

NOMENCLATURE

a_i	coefficients of the polynomial in equation (9)
C_d	total drag factor, $C_{df}+C_{dp}$
$\bar{C}_d$	ratio of drag factors, C_{d2}/C_{d1}
C_{df}	friction drag factor
C_{dp}	form drag factor
c_p	specific heat
$\bar{c}_p$	dimensionless specific heat, $(c_p-c_{p0})/(c_{pm}-c_{p0})$
c_{p0}	specific heat at $T_0 = 273.16$ K
c_{pm}	specific heat at $T_m = 2773.16$ K
d	sphere diameter
h	enthalpy
k	heat conductivity
L_w	length of the sphere wake
Nu	local Nusselt number
$\overline{Nu}$	average Nusselt number, $(1/\pi)\int_0^\pi Nu(\vartheta)\,d\vartheta$
n	refraction index
Pr	Prandtl number
p	pressure
p_s	pressure at sphere surface
R	gas constant, or local curvature radius of light beam
Re	Reynolds number
r	radial coordinate
r_o	outer radius of thermal boundary layer
T	temperature
$\bar{T}$	dimensionless temperature, $(T-T_0)/(T_m-T_0)$
T_K	Sutherland constant
T_s	sphere surface temperature
ΔT	temperature difference between sphere surface and fluid flow
t	time
u_r	radial velocity
u_z	axial velocity
u_ϑ	tangential velocity
x	spacing between spheres
y	distance on the screen
z	axial coordinate.

Greek symbols

α	angle between the light beam and gradient of refraction index n
δ	thermal boundary layer thickness
ε	distribution of interference fringes
ϑ	tangential coordinate, or polar angle along a sphere
ϑ_s	polar angle of separation
λ_0	light wavelength
μ	fluid viscosity
μ_0	fluid viscosity at 273.16 K
ξ, η	calculating coordinate system
ρ	fluid density
τ	viscous stress
Φ	viscous dissipation term of the energy equation
ω_s	sphere surface vorticity.

Subscripts

1	first sphere
2	second sphere
3	third sphere
L	laminar
T	turbulent.

simulation is assured, and so more systematic results can be obtained numerically.

2. EXPERIMENTS

2.1. *Experimental set-up*

Heating spheres of 15 and 25 mm diameter respectively were designed with ceramic bodies and plated chemically with thin films of nickel, and were used for simulating the fluid flow and heat transfer around particles with interaction. The nickel layer was used as both an anti-corrosive layer and a load resistance to generate heat by applying a steady d.c. voltage, $\bar{V}$, at its two poles to simulate the heat released by the combustion of fuel particles. Nickel was chosen because of its good anti-oxidation and stability at high air temperatures of up to 800°C.

Figure 1 shows schematically the fitting and fixing device for adjusting the horizontal and vertical positions of the sphere, or the relative positions of several spheres. In experiments, the testing spheres are to be fitted at the center of the testing part of a 200 × 200 mm square section wind tunnel. The two facing sides of the testing part are fitted with transparent material

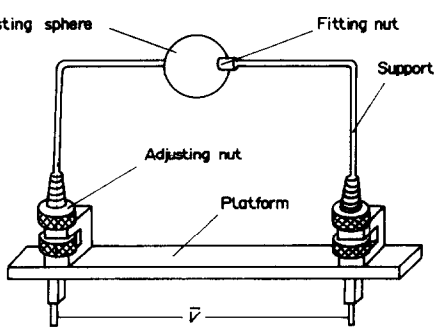

FIG. 1. Fitting device of the sphere.

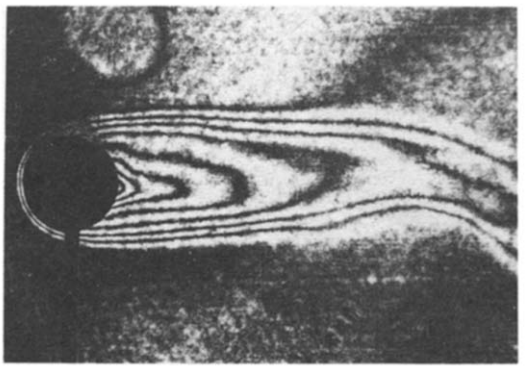

FIG. 2. Typical interference image of air temperature field around a single heating sphere, $Re = 694$, $\Delta T = 514$ K.

to serve as optical windows for laser holographic visualization of the temperature field.

2.2. *Measurement of fluid temperature field with laser holographic interferometry*

An HIF-12 laser holographic interference device made in Germany was used in experiments to measure the fluid temperature fields. The holographic image was taken first for the fluid flow without heat transfer. After development and fixing the image accurately, the object light and reference light were then applied to illuminate the holographic image for the case with heat transfer, and the interference fringes thus produced demonstrated the fluid temperature field in the testing part, which was photographed or recorded successively with a high speed camera, and so the real variation of fluid temperature can be recorded.

Figures 2 and 3 show typical interference images of air temperature fields around single and double heating spheres in tandem respectively. The fringes are almost axially symmetric about the sphere center line along the flow direction, and hence, it may be considered that fluid flow and heat transfer will also be axially symmetric, which will be helpful for experimental data processing and for numerical simulation.

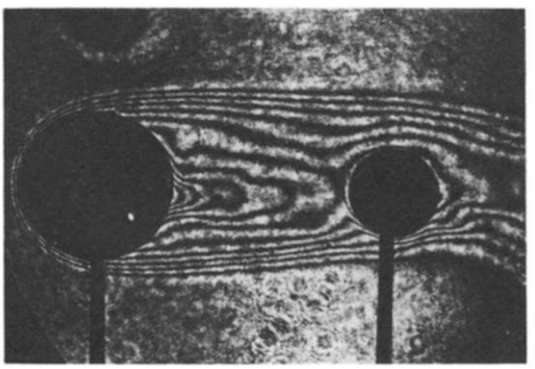

FIG. 3. Typical interference image of air temperature field around two heating spheres in tandem, $Re = 1230$, $\Delta T = 425$ K, $d_2/d_1 = 15/25$, $x = 50$ mm.

Several methods have been discussed for the processing of fringe data of the axial symmetrical interference field in ref. [9], of which a main hypothesis is to neglect the refraction of light, i.e. the light beam remains straight, so that the Abel transformation can be used to get the following formula:

$$\Delta n(r) = -\frac{\lambda_0}{\pi}\int_r^{r_o}\frac{\mathrm{d}\varepsilon(y)/\mathrm{d}y}{\sqrt{(y^2-r^2)}}\mathrm{d}r \qquad (1)$$

where n is the refraction index, ε the distribution of interference fringes, λ_0 the light wavelength and r_o the outer radius of the thermal boundary layer.

In fact, the horizontal incident light beam will bend in the testing part of the axially symmetrical refraction field, as shown in Fig. 4, and hence, the local curvature radius of the light beam, R, will be finite from the Fermat principle of light propagation in heterogeneous media:

$$\frac{1}{R} = \frac{\operatorname{grad} n}{n}\sin\alpha. \qquad (2)$$

Hence, it is suggested here that the trial calculation method [10] can be used to process the interference fringes. First, the temperature distribution $T = T(r)$ in the boundary layer of thickness δ is assumed for trial, from which the distribution of the refraction index, $n(r)$, can be obtained as described in the Appendix. Then, the distribution of interference fringes, $\varepsilon(y)$, is calculated and compared with the experimental one until the calculated results agree well with the experimental results. The thermal boundary layer thickness, δ, can therefore be determined. Obviously, the numerical calculation will be time consuming.

2.3. *Measurement of the sphere surface temperature distribution with infrared scanning technique*

An AGA-780 infrared scanning device made in Sweden was used to determine the temperature distribution of the heating sphere surface. This infrared scanning unit transforms the thermal radiation energy from the object to be measured into electronic visual frequency signals which are amplified and transmitted to the display unit. These signals display thermal images on the screen after being amplified further.

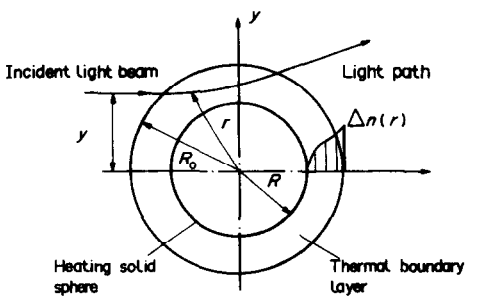

FIG. 4. Real bend light path.

The object temperature can be measured sensitively in the range of -20 to 800°C.

3. NUMERICAL SIMULATION

From experimental visualization, the temperature field and fluid flow around heating spheres in tandem can be assumed as being axisymmetric about the sphere center link line along the flow direction. Hence, the governing equations can be expressed in two-dimensional form. If the body force and heat radiation are both neglected, these equations will be:

$$\frac{\partial \rho}{\partial t}+\frac{\partial(\rho r u_r)}{r\partial r}+\frac{\partial(\rho u_z)}{\partial z}=0 \tag{3}$$

$$\rho\left(\frac{\partial u_r}{\partial t}+u_r\frac{\partial u_r}{\partial r}+u_z\frac{\partial u_r}{\partial z}\frac{u_\vartheta^2}{r}\right)=\frac{1}{r}\left(\frac{\partial(r\tau_{rr})}{\partial r}+\frac{\partial(r\tau_{rz})}{\partial z}\right)-\frac{\tau_{\vartheta\vartheta}}{r} \tag{4}$$

$$\rho\left(\frac{\partial u_\vartheta}{\partial t}+u_r\frac{\partial u_\vartheta}{\partial r}+u_z\frac{\partial u_\vartheta}{\partial z}+\frac{u_r u_\vartheta}{r}\right)=\frac{1}{r}\left(\frac{\partial(r\tau_{r\vartheta})}{\partial r}+\frac{\partial(r\tau_{z\vartheta})}{\partial z}\right)+\frac{\tau_{r\vartheta}}{r} \tag{5}$$

$$\rho\left(\frac{\partial u_z}{\partial t}+u_r\frac{\partial u_z}{\partial r}+u_z\frac{\partial u_z}{\partial z}\right)=\frac{1}{r}\left(\frac{\partial(r\tau_{rz})}{\partial r}+\frac{\partial(r\tau_{zz})}{\partial z}\right) \tag{6}$$

$$\rho\left(\frac{\partial h}{\partial t}+u_r\frac{\partial h}{\partial r}+u_z\frac{\partial h}{\partial z}\right)=\frac{\mathrm{D}p}{\mathrm{D}t}-\frac{p}{\rho}\frac{\mathrm{D}\rho}{\mathrm{D}t}+\frac{1}{r}\left[\frac{\partial}{\partial r}\left(kr\frac{\partial T}{\partial r}\right)+\frac{\partial}{\partial z}\left(kr\frac{\partial T}{\partial z}\right)\right]+\Phi. \tag{7}$$

The Baldwin–Lomax algebraic turbulent model [11] is used to get the turbulent viscosity μ_T. The fluid thermophysical properties such as density, ρ, specific heat, c_p, thermal conductivity, k, Prandtl number, Pr, and viscosity, μ, affected by high temperature differences are estimated from the calculated velocity, pressure and temperature at every iteration using the following relations:

$$\rho = p/RT \tag{8}$$

$$\mu = \mu_L+\mu_T \tag{9}$$

$$\frac{\mu}{Pr}=\frac{\mu_L}{Pr_L}+\frac{\mu_T}{Pr_T} \tag{10}$$

$$\mu_L=\mu_0\left(\frac{T}{T_0}\right)^{1.5}\left(\frac{T_0+T_K}{T+T_K}\right) \tag{11}$$

$$\bar{c}_p=\sum_{i=1}^{10} a_i\bar{T}^{i-1} \tag{12}$$

where $\bar{c}_p=(c_p-c_{p0})/(c_{pm}-c_{p0})$ and $\bar{T}=(T-T_0)/(T_m-T_0)$ are both dimensionless with $T_0=273.16$ K and $T_m=2773.16$ K.

The coordinate conversion is made using the TTM method [12] to transform the given conditions on the real curvilinear boundary to the calculating coordinate boundary conditions of differential equations. With

$$\xi=\xi(z,r) \quad \text{and} \quad \eta=\eta(z,r) \tag{13}$$

the coordinate transformation relations will be:

$$J\cdot\xi_z = r_\eta \tag{14}$$

$$J\cdot\xi_r = -z_\eta \tag{15}$$

$$J\cdot\eta_z = -r_\xi \tag{16}$$

$$J\cdot\eta_r = z_\xi. \tag{17}$$

For the implicit relation:

$$F(\xi,\eta)=F[\xi(z,r),\eta(z,r)] \tag{18}$$

the following formulae will be obtained by the train rule:

$$\frac{\partial F}{\partial z}=F_\xi\cdot\xi_z+F_\eta\cdot\eta_z \tag{19}$$

$$\frac{\partial F}{\partial r}=F_\xi\cdot\xi_r+F_\eta\cdot\eta_r. \tag{20}$$

Substituting the governing equations with the above converting relations, we have the quasi-conservative equations with which the calculations are carried out by use of the SIMPLER method [13]. The corresponding boundary conditions are given as follows:

(a) at the inlet, fluid temperature, magnitude and direction of velocity are given, pressure is obtained by extrapolation with that of the second station;

(b) at the outlet, the pressure is given, temperature and velocity are obtained with the zero gradient condition;

(c) at the symmetrical axis, radial velocity $u_r=0$, while axial velocity u_z, fluid temperature and pressure are obtained with the zero gradient condition;

(d) at the sphere surface, the non-slip isothermal condition is followed;

(e) at the outer boundary, the non-slip isothermal condition is used for the solid surface and the zero gradient condition is used for the free flow boundary.

4. RESULTS AND DISCUSSION

The temperature field around heating spheres can be visualized through the interference fringe distribution and the heat transfer characteristics can be obtained by using the reverse technique to process experimental data. The present experimental ranges are: $Re=300$–1700, temperature difference between sphere surface and air stream, $\Delta T=60$–545°C. On the basis of experiments, numerical simulation is made to serve as an effective means for getting more systematic results.

Figure 5 shows the typical flow fields and isograms

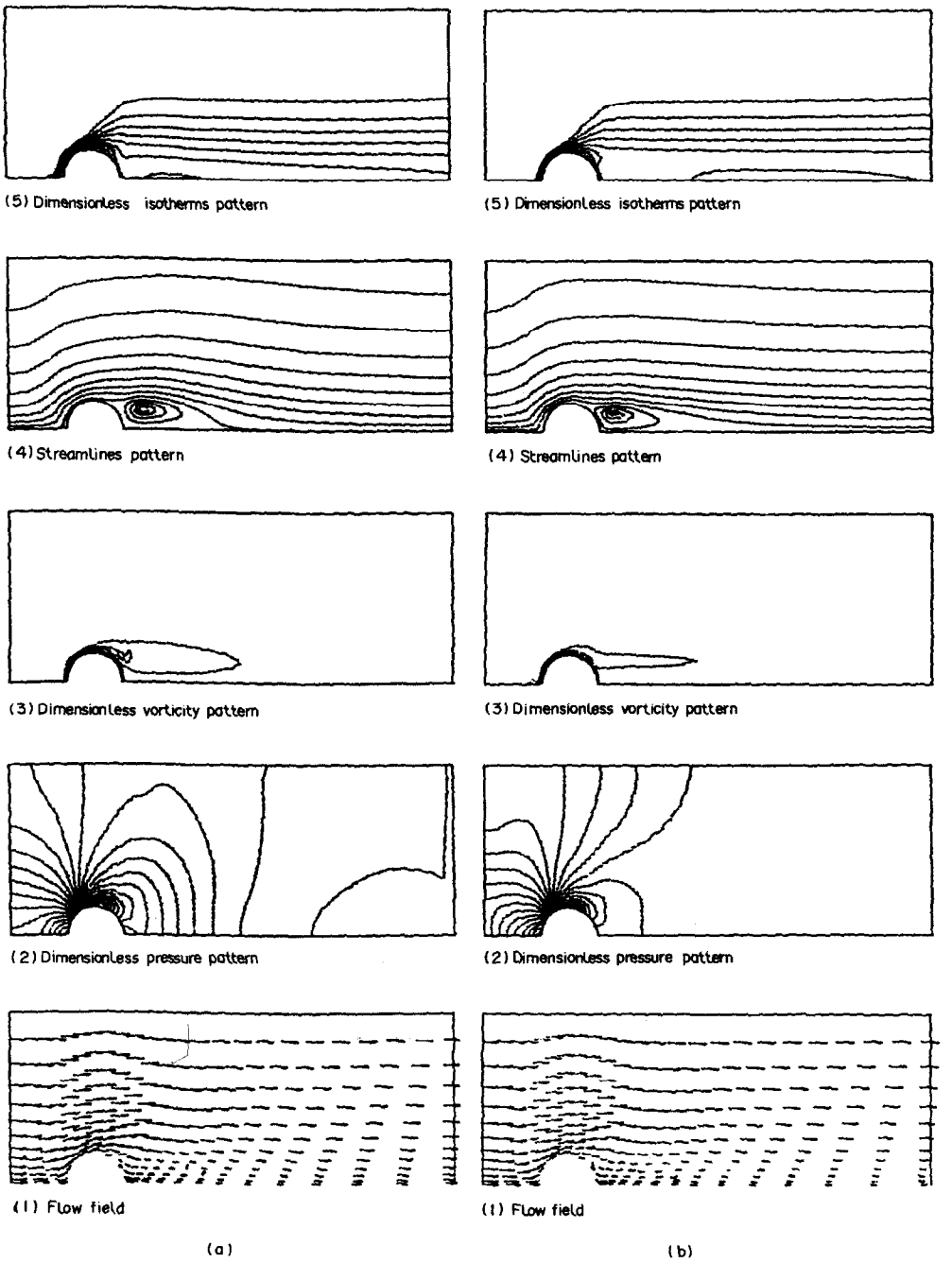

FIG. 5. Flow field and isograms for a single heating sphere. (a) $Re = 694$, $\Delta T = 514$ K, constant thermophysical properties. (b) $Re = 694$, $\Delta T = 514$ K, variable thermophysical properties.

around a single heating sphere for the case of $Re = 694$ and $\Delta T = 512$ K with either variable or constant thermophysical properties. The velocity profile obtained for cases with constant properties is steeper and the size of wake is larger.

Figure 6 shows the comparisons of the curves of Nu, surface pressure, P_s, and surface vorticity, ω_s, for cases of both variable or constant thermophysical properties, from which the data shown in Table 1 demonstrate more clearly that there exists quite obvious differences between them. The numerical results are compared with experimental values in Fig. 7, which indicates the suitability of the cylindrical cell model and the necessity to take fluid physical properties affected by temperature into consideration at high temperature differences.

4.1. *Fluid flow*

It can be seen from Fig. 8 that, for a single heating sphere, the wake length, L_w, increases with increasing

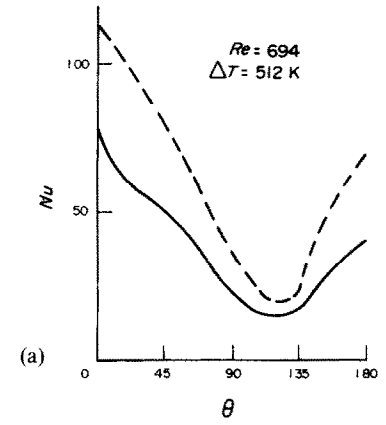

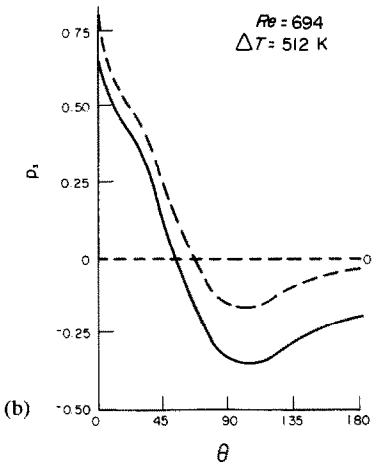

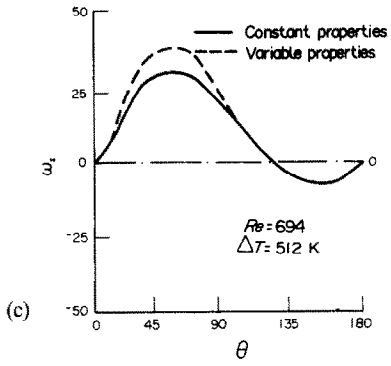

FIG. 6. Numerical results. (——) Variable properties. (- - -) Constant properties. (a) Nu vs ϑ. (b) p_s vs ϑ. (c) ω_s vs ϑ.

Table 1. Effect of variation of thermophysical properties for the case of $Re = 694$, $\Delta T = 512$ K, single sphere

	C_{dp}	C_{df}	C_d	$\overline{Nu}$
Constant properties	0.679	0.239	0.918	58.17
Variable properties	0.817	0.442	1.259	36.60
Deviation (%)	−17	−46	−27	59

Table 2. Effect of ΔT for the case of $Re = 892$, single sphere

	ϑ_s (deg)	L_w/d	C_{dp}	C_{df}	C_d
$\Delta T = 512$ K	126	1.2	0.826	0.334	1.160
$\Delta T = 0$ K	118	1.4	0.810	0.256	1.066
Increment (%)	7	−14.3	2	30	8.8

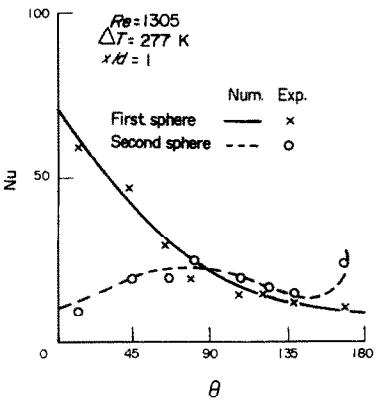

FIG. 7. $Nu = f(\vartheta)$ for two heating spheres with equal diameters in tandem.

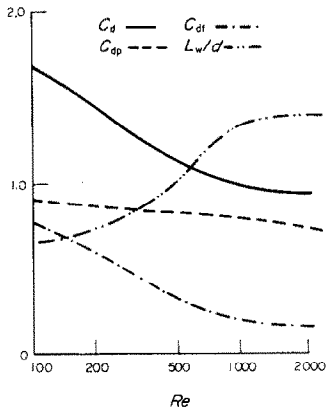

FIG. 8. Flow characteristics for a single sphere.

Re and tends to be stable when Re increases further. The effect of Re on friction drag is larger than that on form drag, so the drag factor is mainly affected by friction. At the same time, the separation point will move downward, i.e. the separation angle, ϑ_s, will increase and the length of the wake will decrease for increasing ΔT, as indicated quantitatively in Table 2.

Figure 9 shows the drag factors of two spheres in tandem changing with the ratio of spacing, x/d. The main part affecting the drag factor of the rear sphere is that of form drag. The curve of C_{d2}/C_{d1} vs x/d is plotted in Fig. 10, from which there is a point where C_{d2}/C_{d1} will be a minimum. The effect of d_2/d_1 on flow is illustrated in Table 3.

Table 3. The effect of d_2/d_1 on the flow characteristics for the case: $Re = 718$, $\Delta T = 277$ K, two contacted spheres in tandem

d_2/d_1	ϑ_{s1} (deg)	ϑ_{s2} (deg)	C_{d1}	C_{d2}	C_{d2}/C_{d1}
15/25	134	149	1.130	0.046	0.041
1/1	127	136	1.021	0.356	0.349
25/15	135	134	0.751	0.635	0.846

Table 4. The effect of x/d on flow characteristics for the case: $Re = 718$, $\Delta T = 277$ K, three spheres in tandem

x/d	C_{d1}	C_{d2}	C_{d3}	C_{d2}/C_{d1}	C_{d3}/C_{d1}
2	1.086	0.332	0.500	0.306	0.460
4	1.147	0.616	0.638	0.537	0.556

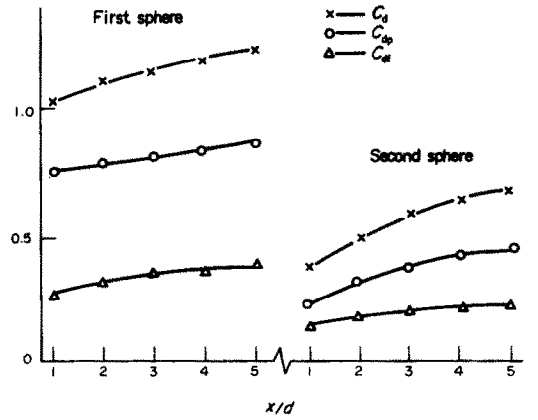

FIG. 9. Drag factors vs x/d for two spheres with equal diameters in tandem.

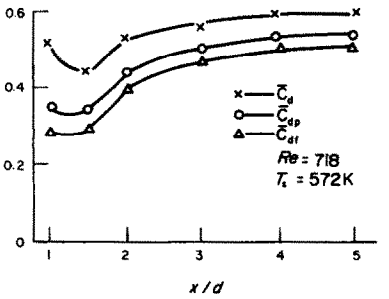

FIG. 10. C_{d2}/C_{d1} vs x/d.

For three spheres with equal diameter in tandem, the flow around the latter two spheres is approximately periodical and the drag factors are closer only when x/d is larger, as shown in Table 4.

4.2. *Heat transfer*

Figures 11 and 12 illustrate that Nu increases with

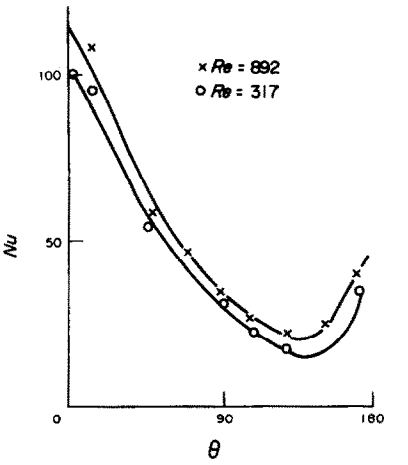

FIG. 11. Nu vs ϑ for air flow around a single heating sphere, $Nu = f(Re, \vartheta)$.

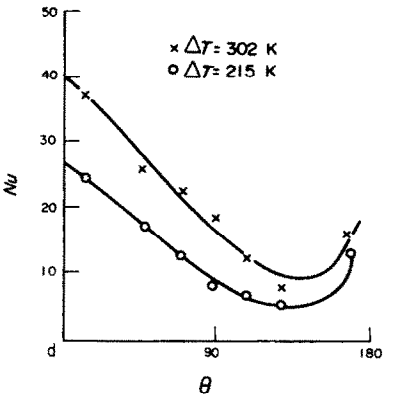

FIG. 12. Nu vs ϑ for air flow around a single heating sphere, $Nu = f(\Delta T, \vartheta)$.

increasing Re and ΔT. Both experimental and numerical results show that there is a polar angle ϑ at which Nu is minimum, and then Nu increases gradually. From the numerical results in Fig. 13, it can be observed more clearly that the polar angle of minimum Nu is coincident with that of zero vorticity (i.e. the separation point). This may be explained as, at the separation point, convective heat transfer resulting from vorticity is zero, and the heat transfer would be conductive. After the separation point, the absolute value of vorticity increases due to the wake circulation, thus making Nu increase gradually.

Figure 2 also shows that the interference fringes extend downward about five times the sphere diameter, i.e. the affected range of temperature wake is quite large. If there is another sphere in the wake, the wake fluid temperature will be further higher than that of inlet flow, so the local Nu thus tends to

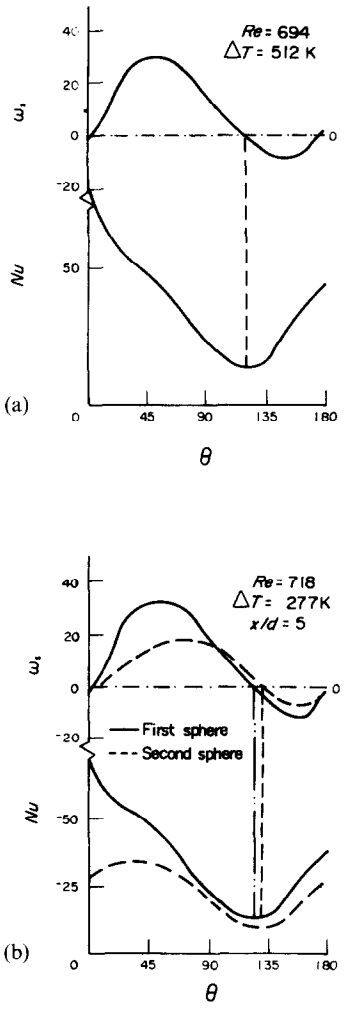

FIG. 13. Nu and ω_s vs ϑ. (a) Single sphere. (b) Two equal diameter spheres in tandem.

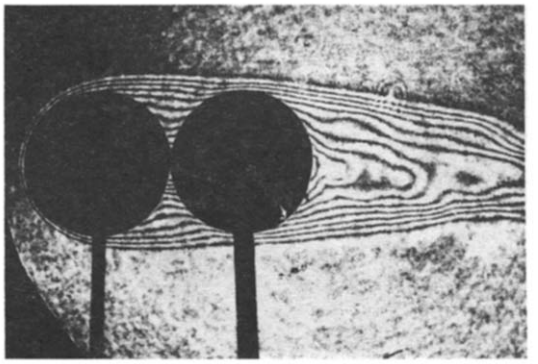

FIG. 14. Typical interference image of air temperature field around two contacted heating spheres in tandem, $Re = 1.47 \times 10^3$, $\Delta T = 386$ K.

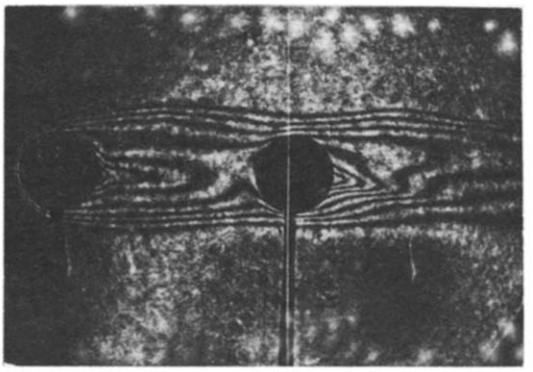

FIG. 15. Typical interference image of air temperature field around two heating spheres in tandem, $Re = 552$, $\Delta T = 462$ K, $x/d = 3$.

decrease. The spacing between spheres in tandem indicates whether the latter sphere is in the wake of the former one, or which position in the wake the latter one takes.

Figures 14 and 15 are typical interference images for different spacings. Table 5 shows that $\overline{Nu}$ of the first sphere is nearly constant when $x/d \geqslant 3$ for the case of two equal diameter spheres in tandem. Figure 16 shows that there is a minimum point for $\overline{Nu}_2/\overline{Nu}_1$ when x/d is about 2, which shows that the wake effect of the former sphere on the latter sphere will be maximum. However, the affected range of the sphere is limited, so the latter sphere tends to appear as the case of a single sphere if $x/d > 2$, and both the former and latter spheres can be treated as two single spheres when $x/d \geqslant 5$.

Figures 3 and 17 show the interference fringe distribution of two spheres in tandem with different ratios of sphere diameters d_2/d_1 respectively, from which the ratio of sphere diameters would also be an

Table 5. The effect of x/d on $\overline{Nu}_1$, and $\overline{Nu}_2$ for the case: $Re = 718$, $\Delta T = 277$ K, two spheres in tandem, $d_2/d_1 = 1$

	x/d				
$\overline{Nu}_1$	27.34	32.11	33.46	33.41	33.55
$\overline{Nu}_2$	15.90	17.23	18.12	21.67	22.86

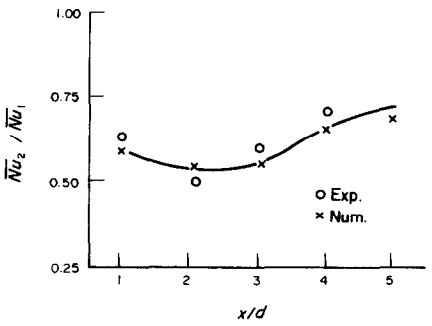

FIG. 16. $\overline{Nu}_2/\overline{Nu}_1$ vs x/d.

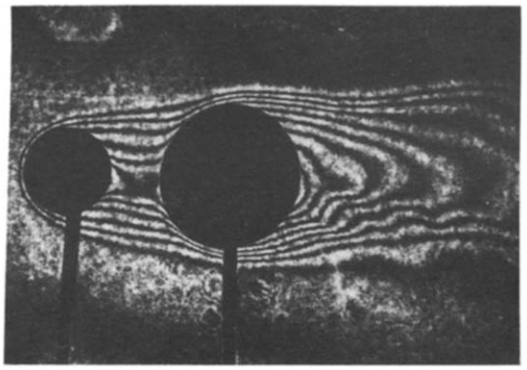

FIG. 17. The interference image of air temperature field around two heating spheres in tandem, $Re = 345$, $\Delta T = 332$ K, $d_2/d_1 = 25/15$, $x = 30$ mm.

important affecting parameter on the fluid flow and heat transfer. When $d_2/d_1 < 1$, the spacing between spheres must be larger to neglect the effect of the former sphere on the latter sphere and $\overline{Nu}_2/\overline{Nu}_1$ increases with increasing distance between spheres. When the ratio $d_2/d_1 > 1$, the distance at which the mutual interaction could be neglected may be less, and hence, there exists a special case for $\overline{Nu}_2/\overline{Nu}_1$ being a minimum at certain sphere spacing.

It should be noted that Nu of the front sphere decreases monotonously when two spheres in tandem are in contact with each other for every sphere diameter ratio. It is difficult for the wake of the former sphere to extend because of the hinder part of the latter sphere; the wake region and its strength for the first sphere are very small behind the separation point, so the convective heat transfer is weak there, and a 'dead region' will exist where the temperature is higher by the two-fold heating of the two spheres. Of course, the wake is also heated directly by the contacted second sphere, the fluid temperature in the wake will be higher and the heat transfer rate should be weakened further. This may explain why Nu of the former sphere decreases monotonously along the polar angle ϑ and is minimum at the contacting point.

Figure 18 shows the interference image and Nu for three heating spheres with equal diameters in tandem. It can be seen that the heat transfer characteristics of the first sphere are similar to those of a single sphere, and the local heat transfer rate distribution has a similar tendency for the latter two spheres, although the Nu values of the third sphere are less than those of the second sphere.

As shown in Table 6, the $\overline{Nu}$ values of three spheres with equal diameter in tandem decrease sphere by sphere. It should be pointed out that the numerical simulation is carried out without consideration of the effect of existing thermal radiation, and hence, the predicted results will overestimate the air temperature gradient near the sphere surface, i.e. larger $\overline{Nu}$ values than experimental ones. In this respect, radiation should also be taken into consideration for the case of high temperature difference.

Table 6. The comparison of numerical and experimental results for the case: $Re = 948$, $\Delta T = 422$ K, $x/d = 2$, three spheres in tandem

Results	$\overline{Nu}_1$	$\overline{Nu}_2$	$\overline{Nu}_3$
Numerical	35.70	20.83	17.81
Experimental	29.45	17.34	15.74

5. CONCLUSIONS

(1) The temperature field and heat transfer around the heating spheres in tandem are measured successfully with a non-contacting method, i.e. by measuring the fluid temperature field by the laser holographic technique and then measuring the sphere surface temperature distribution by infrared thermovision. It is thus possible to measure the local heat transfer characteristics of larger particles, which is preferable to measuring real suspended particles or particles with interaction, and the experimental results

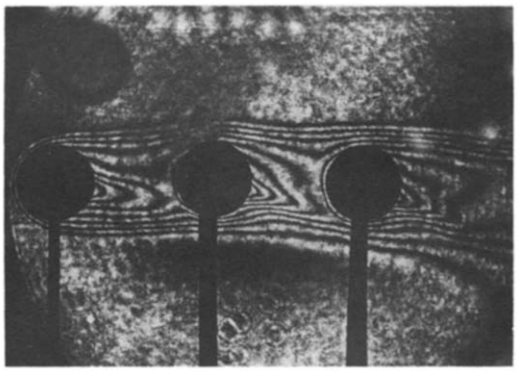

(a)

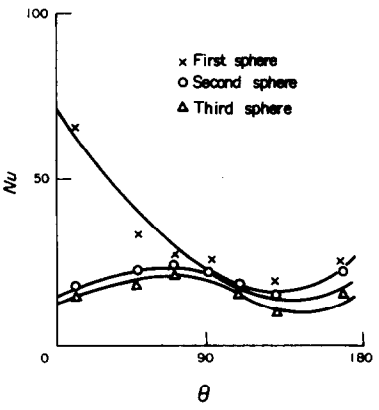

(b)

FIG. 18. The interference image of air temperature field (a) and Nu (b) for three heating spheres with equal diameter, $Re = 948$, $\Delta T = 426$ K, $x/d = 23$.

are more feasible than those obtained by the conventional contacting method.

(2) Over quite a wide range, the heat transfer characteristics affected by various parameters such as the Reynolds number, Re, the temperature difference between the sphere and fluid flow, ΔT, the spacing between spheres, x, and the ratio of sphere diameters, d_2/d_1, are obtained for the heating solid spheres with equal or unequal diameters. These results will be valuable to study further the suspended combusting particles.

(3) The fluid flow and heat transfer around heating spheres in tandem are simulated numerically and the results are coincident with experimental ones. Both the constant and variable fluid thermophysical properties have been used to analyze the effect of temperature difference. It is clear that the numerical results are closer to experimental results if variable thermophysical properties are taken into consideration, especially for the case of high temperature differences. In practice, thermal radiation should be considered, which will be investigated and reported later.

(4) Both experimental and numerical results show that Nu increases with increasing Re and ΔT, and decreases with increasing spacing between spheres, x, and the ratio of sphere diameters, d_2/d_1, i.e. the interacting effect between heating spheres weakens with increasing x and d_2/d_1.

REFERENCES

1. R. Clift, J. R. Grace and M. E. Weber, *Bubbles, Drops, and Particles*. Academic Press, New York (1978).
2. Q. Hassonjee, P. Ganatos and R. Pfeffer, A strong-interaction theory for the motion of arbitrary three-dimensional clusters of spherical particles at low Reynolds number, *J. Fluid Mech.* **197,** 1–37 (1988).
3. P. N. Rowe and G. A. Henwood, Drag forces in a hydraulic model of a fluidized bed—part I, *Trans. Instn Chem. Engrs* **39,** 43–54 (1961).
4. K. C. Lee, Aerodynamic interaction between two spheres at Reynolds numbers around 10^4, *Aeronaut. Q.* **Feb.,** 371–385 (1978).
5. Y. Tsuji, Y. Morikawa and K. Terashima, Fluid–dynamic interaction between two spheres, *Int. J. Multiphase Flow* **8,** 71–81 (1982).
6. E. M. Sparrow and R. F. Prieto, Heat transfer coefficient and patterns of fluid flow containing spheres at various angles of attack, *J. Heat Transfer* **105,** 48–55 (1983).
7. T. Liu, Hydrodynamic and heat transfer research for gas-sphere flow around heating solid spheres in tandem, Doctoral Thesis, Tsinghua University, Beijing, China (1990).
8. R. Tal (Thau) and W. A. Sirignano, Heat transfer in sphere assemblages at intermediate Reynolds numbers: a cylindrical cell model, ASME Paper 81-WA/HT44 (1981).
9. W. Hauf and U. Grigull, Optical methods in heat transfer, *Adv. Heat Transfer* **6,** 133–366 (1972).
10. S. Y. Huang and J. B. Yang, *The Optical Measurement of Thermophysical Parameters*. Press of Huazhong Institute of Technology (in Chinese) (1985).
11. B. S. Baldwin and H. Lomax, Thin layer approximation and algebraic model for separated turbulent flows, AIAA Paper 78-257 (1978).
12. J. F. Thompson, F. C. Thames and C. W. Mastin, Boundary-fitted curvilinear coordinate systems for solution of differential equations containing any number of arbitrary two-dimensional bodies, *J. Comp. Phys.* **15,** 299–319 (1974).
13. S. V. Patankar, *Numerical Heat Transfer and Fluid Flow*. McGraw-Hill, New York (1980).

APPENDIX

Figure A1 shows the path of light passing through the axially symmetrical thermal boundary layer to the photographic plate, where MM' is the interference plane. The light goes into the thermal boundary layer, then through the fluid with the refraction index n_F, the measuring window with n_G, and ambient air with n_L to the object lens O, with which the image is produced on the plate. It is clear that, if the light is not deflected, the object light, i.e. the measuring light entering from P, would interfere with the relative light entering from P at A on plane MM' and the image of A would form at A'. In fact, light will inflect in the thermal boundary layer, so the object light entering from P will deviate with P', pass through fluid with reflection angle γ', and enter the window of the testing section at P'', where the light reflects with refraction angle γ'' and leaves from the window at P''' with γ'''. Extending the light radiating from P''' back to the plane MM', the point B is obtained. Therefore, the reflected light, displayed at B' on the plate by the object lens O, looks like that radiated from point B. Hence, the line segment $\overline{A'B'}$ is related to the line segment $\overline{AB}$ by the optical system which could be considered as location error during the processing of the interference image.

The object light entering from P interferes with the relative light entering from E, which is parallel to the light axis and passes through point B. The object light path is equal to the relative light path before P and Q. According to the property of an ideal lens, the light paths are equal for all the light beam entering from B and focusing at B', so P''' and Q''' must locate at the circular arc with point B at the center. For the object light, the light path from P to P''' is

$$L_0 = \int_P^{P'} n \cdot \mathrm{d}s + \overline{P'P''} \cdot n_F + \overline{P''P'''} \cdot n_G. \tag{A1}$$

For the relative light, the light path from Q to Q''' is

$$L_R = \overline{QQ'} \cdot n_F + \overline{Q'Q''} \cdot n_G + \overline{Q''Q'''} \cdot n_L. \tag{A2}$$

Interference fringes are produced since there is an optical path difference $L_0 - L_R$, that is

$$s \cdot \lambda_0 = L_0 - L_R. \tag{A3}$$

The track of $\overline{PP'}$ should be obtained to calculate $\int_P^{P'} n \cdot \mathrm{d}s$ as follows.

First, a refraction index field is assumed, so the gradient of refraction index and the angle between the incident light

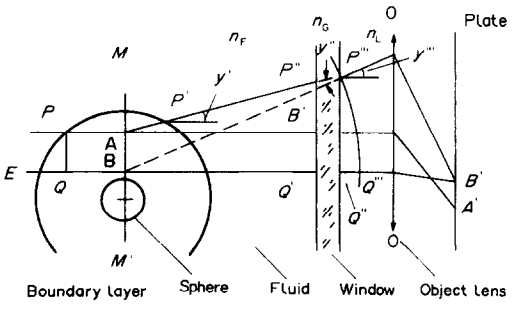

FIG. A1. Real light path.

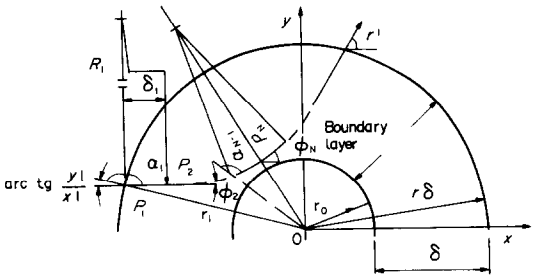

FIG. A2. Schematic diagram of solution for integral path $\int_P^{P'} n \cdot ds$.

and the gradient is known. Then, the thermal boundary layer is divided into many concentric rings with small enough increments. From an initial point P_1, the intersecting point of the light with the next ring can be calculated. The sum of light paths for every ring $n_i \cdot \Delta s_i$ is the integral path. Take Fig. A2 for example and assume the incident light enters into the thermal boundary layer horizontally at $P_1(x, y)$, so it can be found that

$$\alpha_1 = \pi - \arctan\frac{y_1}{x_1} - \phi_1 \tag{A4}$$

where ϕ_1 is the incidental angle of light which is zero while the light enters horizontally. If the refraction index and its gradient are given, the curvature radius of the light R_1 can be calculated. So the optical path in the first ring can be obtained. Then a vertical line is drawn from P_1 and a circular arc is drawn with the radius of R_1, which intersects with the next ring at P_2 and has the arc length of Δs_1. So, $n_1 \cdot \Delta s_1$ can be obtained.

The incident angle at point P_2, ϕ_2, can be calculated from the curvature radius R_1 and the arc length Δs_1, i.e.

$$\phi_2 = \Delta s_1 / R_1 + \phi_1. \tag{A5}$$

We can start the next step of drawing and so on until the optical path of light is vertical to the gradient of refraction index at P_N, where the distance between the light and the point O is a minimum, i.e. P_N is located at the symmetrical part of the optical path. Then $\Sigma n_i \cdot \Delta s_i$ and the angle of light radiating out from the boundary layer, γ', and thus the 'location error' can be turned out for determining the interference fringes on the photographic plate.

RECHERCHES SUR L'HYDRODYNAMIQUE ET LE TRANSFERT POUR L'ECOULEMENT D'UN FLUIDE AUTOUR DE SPHERES CHAUDES EN TANDEM

Résumé—Le champ de température et le transfert thermique pour un écoulement de fluide autour des sphères solides chauffées en tandem ont été mesurés par interférométrie holographique laser et une technique de scanner infrarouge. Les caractéristiques de transfert thermique pour les sphères solides chaudes avec des diamètres égaux ou non, sensibles à plusieurs paramètres comme Re, ΔT, x et d_2/d_1, sont obtenues en détail expérimentalement. La simulation numérique est faite pour prédire des conditions de propriétés physiques constantes et variables. Les résultats numériques sont très proches de ceux de l'expérimentation et ils montrent que l'on peut obtenir plus de résultats systématiques et audio-visuels.

UNTERSUCHUNG DER HYDRODYNAMIK UND DES WÄRMEÜBERGANGS BEI DER STRÖMUNG EINES FLUIDS UM BEHEIZTE, HINTEREINANDER ANGEORDNETE KUGELN

Zusammenfassung—Es wird das Temperaturfeld und der Wärmeübergang bei der Strömung eines Fluids um beheizte, hintereinander angeordnete Kugeln mittels holografischer Interferometrie sowie Infrarot-Aufnahmen bestimmt. Der Wärmeübergang an beheizten Kugeln gleichen und ungleichen Durchmessers wird in Abhängigkeit von verschiedenen Parametern wie Re, ΔT, x und d_2/d_1 ausführlich experimentell untersucht. Die numerische Simulation wird durchgeführt, um den Einfluß von konstanten und variablen Stoffeigenschaften voraussagen zu können. Die numerischen Ergebnisse stimmen gut mit den experimentellen Werten überein. Sie zeigen, daß mehr systematische und audiovisuelle Ergebnisse erhalten werden können.

ИССЛЕДОВАНИЕ ГИДРОДИНАМИКИ И ТЕПЛОПЕРЕНОСА ПРИ ОБТЕКАНИИ ПОТОКОМ ЖИДКОСТИ ПОСЛЕДОВАТЕЛЬНО СОЕДИНЕННЫХ НАГРЕВАЕМЫХ СФЕР

Аннотация—С использованием методов лазерной голографической интерферометрии и инфракрасного сканирования определяются температурное поле и теплоперенос при обтекании потоком жидкости последовательно соединенных нагреваемых сфер из твердого материала. Экспериментально определяются характеристики сфер с одинаковыми и различными диаметрами при различных значениях таких параметров, как Re, ΔT, x и d_2/d_1. Проводится численное моделирование для постоянных и переменных физических свойств. Численные результаты хорошо согласуются с экспериментальными данными.